ISSN: 2688-8645

Design of Three-Axis Orthogonal Magnetic Gradient Sensor based on Differential Structure

Qijun Wang [1], Can Su [2], Hang Liu [3] and Rui Zhou [1]

[1] School of Petroleum and Natural Gas Engineering, Southwest Petroleum University, Chengdu, Sichuan, 610000, China

[2] School of Mechanical and Electrical Engineering, Southwest Petroleum University, Chengdu, Sichuan, 610000, China

[3] School of Electrical and Information Engineering, Southwest Petroleum University, Chengdu, Sichuan, 610000, China

Abstract

To address the challenges faced by traditional fluxgate magnetic gradient meters in achieving multi-axis synchronous measurement, such as orthogonality among the three axes, channel consistency, and structural integration, a highly integrated magnetic gradient sensor design based on a center-symmetric orthogonal structure is proposed. The design integrates the three-axis differential sensing units into a compact whole through an integrated three-dimensional orthogonal coil frame, achieving a high degree of physical parameter matching among the channels. On this basis, combined with the reverse series differential detection mechanism and multi-channel synchronous processing circuit, the system's ability to suppress common-mode interference and signal consistency is effectively enhanced. The paper elaborates in detail on the sensor's structural design, working principle, parameter optimization, and signal processing flow. The effectiveness of the design in improving channel consistency and enhancing orthogonal measurement accuracy is verified through finite element simulation.

Keywords

Magnetic Gradient Sensor; Three-dimensional Orthogonality; Structural Design; Integrated Signal Processing Circuit; Finite Element Analysis.

1. Introduction

The magnetic gradient is a key indicator of how the magnetic field varies in a given direction; it is defined as the ratio of the magnetic field values at two points to the distance between them. Compared to the total field, the magnetic gradient exhibits distinct spatial directionality and offers exceptional resolution for magnetic anomalies [1]. Magnetic gradient measurement is a key technology in fields such as geophysical exploration, industrial wastewater monitoring, target localization, and fundamental physics research. High-precision magnetic gradient sensing, as the core component of this technology, directly determines the accuracy and reliability of the detection system. Therefore, the development of magnetic gradient sensors with high stability and strong resistance to interference holds significant theoretical value and practical importance for advancing scientific and technological progress in the aforementioned fields.

Among the various magnetic measurement technologies, fluxgate sensors have become one of the mainstream solutions for gradient measurement due to their moderate cost, high reliability, high resolution, and ability to directly measure vector magnetic fields. Traditional fluxgate gradient sensors typically consist of two spatially separated fluxgate probes, and the magnetic field gradient is estimated by calculating the difference between the outputs of the two probes.

In recent years, researchers have focused on improving this configuration through algorithmic corrections and structural optimization. In terms of algorithm calibration, Yang Zhicheng et al. [2] established an error model to address issues such as non-orthogonality, sensitivity inconsistencies, zero bias, and misalignment between the two sensors in three-axis fluxgate sensors. They proposed a linear least-squares parameter identification method based on the principle of short-term invariance of the geomagnetic vector magnitude, and further employed multiple linear regression to identify the relative position parameters of the two sensors. Gao Xiang et al. [3] developed correction models for the yaw error of magnetic gradientometers from the perspectives of self-calibration and cross-calibration, using the least squares method to compensate for sensor zero-point bias, sensitivity, and non-orthogonal errors. In terms of structure, Li Qingzhu et al. [4] employed a cross-shaped frame, with sensors on each arm capable of sliding within guide rails to adjust the baseline distance, aiming to measure multi-order magnetic gradient tensors via variable baseline; Li Zhipeng et al. [5] used two parallel straight-bar frames, with the magnetic cores connected end-to-end to form a ring-shaped structure, aiming to achieve unidirectional gradient measurement; Zhang Fuzhong et al. [6] employed six amorphous wire probes arranged in three groups along orthogonal coordinate axes, configured in reverse series to achieve gradient measurements; while these methods have made some progress in structural optimization and algorithmic calibration, discrete probes still face challenges such as difficulty in matching parameters between channels and limited common-mode rejection capability when performing three-dimensional orthogonal measurements. To address these challenges, most existing technologies focus on optimizing algorithms through software design to process output data. However, these methods do not fundamentally alter the sensor’s physical structure, leading to performance bottlenecks. In contrast, innovations in the sensor’s physical structure hold the promise of physically suppressing environmental interference, thereby breaking through performance limits.

To address the aforementioned technical challenges, this paper introduces an innovative approach at the level of sensor physical structure, proposing a design scheme for a three-axis orthogonal magnetic gradient sensor based on a differential structure. The core of this design lies in the use of a highly integrated, centrally symmetric three-dimensional orthogonal coil framework combined with a differential coil structure. This design aims to overcome the shortcomings of traditional discrete probes by addressing the issue at the source of the physical structure. The core innovations of this paper are as follows: A highly integrated, centrally symmetric three-dimensional orthogonal coil framework is proposed. The three-dimensional structure is orthogonal in pairs along the X, Y, and Z axes, thereby avoiding errors caused by structural non-orthogonality. By mechanically integrating the three-axis sensing units at a single reference point, parameter consistency is ensured at the geometric level, laying the physical foundation for common-mode rejection; Combined with a differential detection configuration using reverse-series-connected receiving coils, this design achieves first-order physical suppression of uniform environmental field interference, significantly enhancing the sensor’s stability and anti-interference capability; to address the inherent channel mismatch issues of traditional discrete circuits, a multi-channel parallel processing integrated signal conditioning circuit has been designed that is highly compatible with the aforementioned sensor structure. This circuit employs a channel-based, integrated strategy to achieve synchronous, symmetrical processing of three-axis differential signals, effectively preventing crosstalk between channels and ensuring system consistency and reliability.

2. Sensor Body Design and Operating Principles

2.1. Overall Structural Design

The cornerstone of the sensor's performance lies in its integrated mechanical and electromagnetic structure, which achieves intrinsic symmetry and stability in electromagnetic performance through a precision-engineered, monolithic mechanical design. As shown in Figure 1, the core of the sensor is a strictly centrally symmetric, three-dimensional orthogonal magnetic gradient coil framework. This structure integrates six sensing elements into a single unit, ensuring that critical parameters—such as the magnetic core and coils—remain highly consistent immediately after manufacturing. This inherent consistency causes environmental interference to manifest as common-mode signals on the sensing units, providing the prerequisites for differential detection. At the same time, the integrated structural design prevents changes in the relative positions of discrete components caused by minute deformations or vibrations, ensuring the long-term stability of the measurement reference.

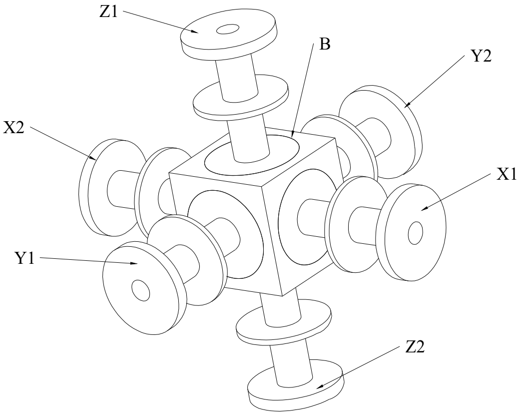

Fig 1. Schematic diagram of the three-dimensional coil skeleton structure

2.2. Mechanism of Differential Detection

Differential detection is key to achieving high stability in sensors. Its effectiveness stems from precise coil design and connection methods. Figure 2 illustrates the overall structure of the sensor and the coil winding configuration.

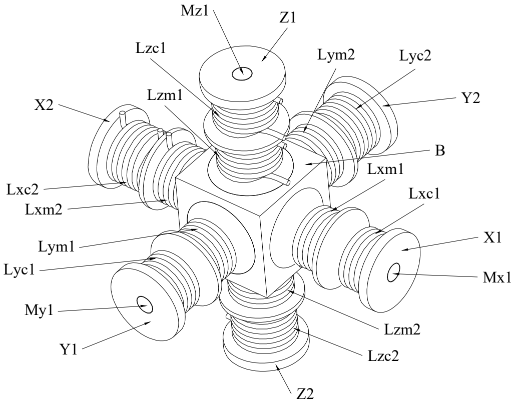

Fig 2. Schematic diagram of three-dimensional orthogonal sensor structure

The connection rules for the coils in each axis are as follows: the excitation coils near the center point O are connected in series in the same direction to ensure excitation consistency; the receiving coils far from the center point O are connected in series in opposite directions to form a differential bridge, thereby enabling signal extraction and common-mode rejection.

Under ideal conditions, the sensor excitation signal is:

$$H = H_m \ \cos 2\pi f \tag{1}$$

In the equation: Hm is the amplitude of the excitation signal; f is the frequency of the excitation signal.

The magnetization curve of the core is shown in Figure 3. Since the excitation field is a function of time, the magnetic permeability also varies with time. Furthermore, because the excitation field is directional while the magnetic permeability is isotropic, the magnetic permeability is an even function of time. The Fourier series expansion of the core's magnetic permeability is given by [1]:

$$\mu(t) = \mu_0 \ + \sum_{n=1}^{+\infty} \mu_{2n} \cos 4n\pi ft \tag{2}$$

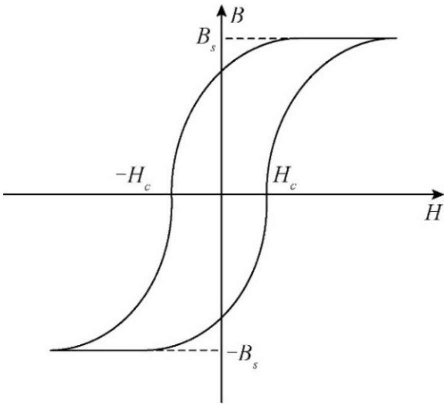

Fig 3. Magnetization curve

In the equation: μ_0 represents the constant component of the magnetic permeability; μ_2_n represents the amplitude of each even-order harmonic after decomposing the magnetic permeability. Based on Faraday's law of electromagnetic induction, and taking into account the decomposition of the magnetic core's permeability, the induced signal at the flux gate caused by the magnetic field under test is given by:

$$E(H_0) = -4\pi fNSH_0 \times \sum_{n=1}^{+\infty} n\mu_{2n} \sin 2n\pi ft \tag{3}$$

In the equation, H_0, N, and S represent the magnetic field under test, the number of turns in the sensing coil, and the cross-sectional area of the magnetic core, respectively. When a uniform magnetic field exists in the space, the induced electromotive forces of the two series-connected receiving coils in opposite directions cancel each other out, resulting in a zero output and achieving common-mode rejection; when an axial gradient is present, the magnetic fields at the two cores are unequal (denoted as H1 and H2, respectively), and the coils output a voltage signal proportional to the magnetic field gradient. The output signal of the magnetic gradient meter is:

$$\begin{aligned} G &= -\frac{4\left[H_1 - (-H_2)\right]}{d} \pi fNS \times \sum_{n=1}^{+\infty} n\mu_n \sin 2n\pi ft \\ &= -\frac{4\left[H_1 + H_2\right]}{d} \pi fNS \times \sum_{n=1}^{+\infty} n\mu_n \sin 2n\pi ft \end{aligned} \tag{4}$$

Here, d represents the distance between the two measurement points. As shown in Equation (4), the effective signal is superimposed and amplified. Therefore, this structure exhibits high sensitivity to gradient fields and high suppression of common-mode interference.

2.3. Design of a Fluxgate Sensor Probe

Based on the requirements for insulation, low magnetic permeability, high stability, and excellent mechanical properties, and after a comprehensive comparison of materials such as polyetheretherketone (PEEK), polytetrafluoroethylene, epoxy resin, and polystyrene, this design selects PEEK as the matrix material. Its superior overall performance—including high insulation, low magnetic permeability, fatigue resistance, and high stiffness—meets the design requirements.

To improve sensor accuracy and resolution, the electromagnetic parameters of the core material must be stable; it is generally considered preferable for the anisotropy constant and linear magnetostriction coefficient to be as low as possible [7][8]. When selecting core materials, criteria include high magnetic permeability, low coercivity, low magnetostriction coefficient and Barkhausen noise, an appropriate saturation field strength, high frequency stability, and high magnetic permeability [9]. Materials such as silicon steel, ferrites, permalloy, amorphous alloys, and nanocrystalline alloys are all suitable for magnetic applications. This design employs a high-permeability material with a relative permeability greater than 10,000. After a comprehensive comparison of the relevant parameters of several materials, as shown in Table 1, permalloy was selected as the core material for this design.

Table 1. Comparison of core material parameters

Magnetic core material	Relative magnetic permeability	Resilience (A/m)	Saturated magnetic field strength(T)	Magnetostrictive coefficient
Silicon steel	1500	40	2.03	10×10^{-6}
Ferrite	3000	8	0.5	1×10^{-6}
Pomo alloy	20000	0.5	0.74	0.1×10^{-6}
Amorphous alloy	10000-50000	2-10	1.2-1.6	$10\text{-}30\times10^{-6}$
Nanocrystalline alloy	30000-100000	0.5-3	1.2-1.3	2×10^{-6}

The coil design primarily consists of excitation and receiving coils along the X, Y, and Z axes. All coils are wound with 0.2 mm enameled wire. The number of turns in the excitation coil affects the strength of the excitation magnetic field and the coil inductance. According to the literature, based on the weak magnetic field of a fluxgate sensor, the number of turns in the excitation coil can be expressed as [10]:

$$N_1 = \frac{H_{\mathrm{m}}}{f_1 \pi \mu A H_s} \tag{5}$$

where μ is the magnetic permeability of the core, A is the cross-sectional area of the coil, and Hs is the saturation magnetic field of the core;

Based on the relevant parameters of the selected Permalloy, the number of turns in the excitation coil was determined to be 200. When determining the number of turns N2 in the induction coil, both the probe's sensitivity and noise must be taken into account. Since the induction coil is always located on the outermost layer of the probe, N2 can be easily adjusted after the prototype is fabricated. Although increasing N2 can improve sensitivity, it simultaneously increases noise. If the coil is made thicker, it leads to increased magnetic leakage, causing noise to grow faster than the signal, resulting in a decrease rather than an increase in the signal-to-noise ratio [11].

3. Signal Processing System Design

3.1. System Architecture and Integration Strategy

The overall architecture of the signal processing system is shown in Figure 4, which employs a channelized, integrated design strategy. Three independent, symmetrical measurement channels are designed to prevent crosstalk between channels and ensure consistent performance. The system comprises drive, signal processing (including amplification, demodulation, and filtering), and analog computation modules, which are responsible for exciting the sensors and processing the received signals, ultimately converting the gradient signals into voltage. This design utilizes a highly integrated dedicated chip, with all internal components fabricated on a single silicon die. This provides excellent consistency and temperature stability, significantly reduces the number of external components, and enhances system reliability and compactness.

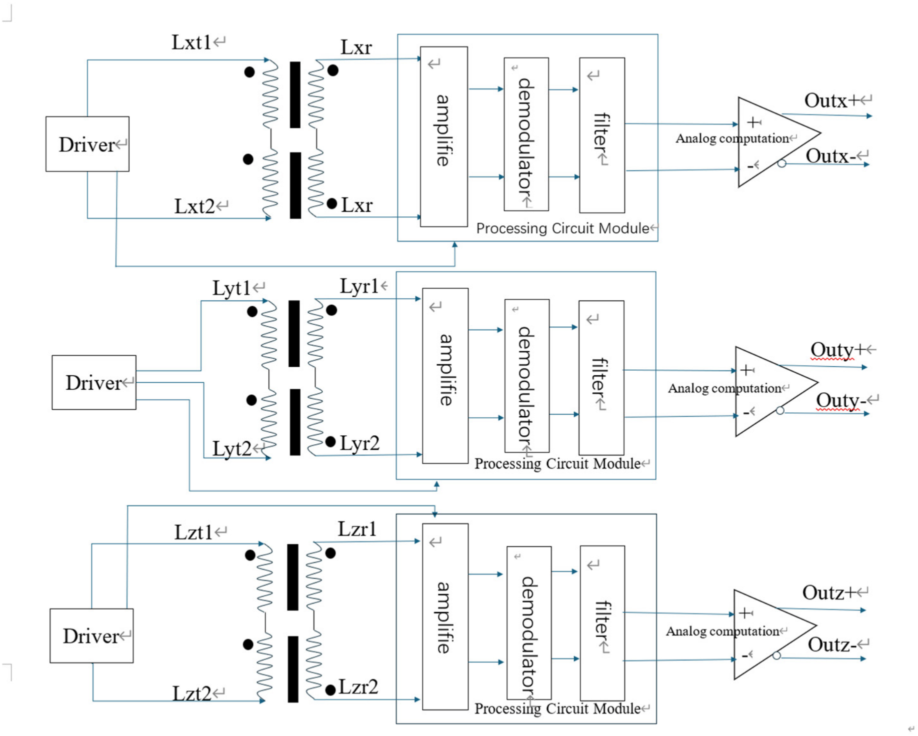

Fig 4. Hardware structure and function diagram

3.2. Design of Drive Circuits

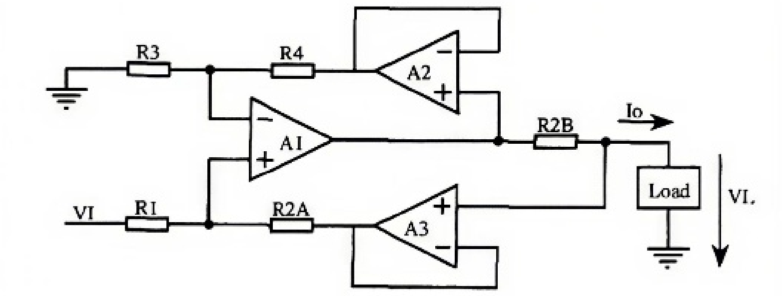

Fig 5. VCCS circuit diagram

The purpose of the excitation drive circuit is to generate a high-stability AC signal to drive the coil. This design employs a highly stable signal source based on DDS technology [12], which achieves frequency stability at the ppm level and effectively suppresses demodulation errors caused by frequency drift. To ensure that the magnetic core periodically enters a state of deep saturation, the scheme abandons constant-voltage drive—which is susceptible to temperature-induced drift in coil impedance—and instead adopts a voltage-controlled current source (VCCS) constant-current drive strategy [13], as shown in Figure 5. This strategy ensures that the output current is determined solely by the high-stability reference source and the set resistor, independent of the load impedance, thereby guaranteeing the stability of the excitation magnetic field's amplitude and fundamentally eliminating sensitivity errors.

3.3. Signal Conditioning Circuit

The signal processing circuit employs a three-stage precision design to convert weak differential signals into high-precision DC voltages. First, the preamplifier, with its high input impedance, low noise, and high common-mode rejection ratio, ensures distortion-free signal acquisition and further suppresses common-mode interference. Second, the phase-sensitive demodulator multiplies the amplified signal by a phase-adjustable, in-phase reference signal to accurately extract the DC component reflecting the amplitude and polarity of the gradient field, while significantly suppressing irrelevant noise. Finally, the low-pass filter extracts the DC component and attenuates residual high-frequency components; its cutoff frequency is set through an optimized trade-off between noise level and response speed. Specifically, taking the excitation and reception coils on the X-axis coil frame as an example, the excitation pins of the integrated chip are connected to the Lxt1 point of the first excitation coil Lxm1 and the Lxt2 point of the second excitation coil Lxm2, respectively, as shown in Figure 5. The chip's receive pins are connected to points Lxr1 of the first receive coil Lxc1 and Lxr2 of the second receive coil Lxc2, respectively, to amplify, filter, and demodulate the signal. The signal is then processed through analog operations to produce the Outx+ and Outx- outputs.

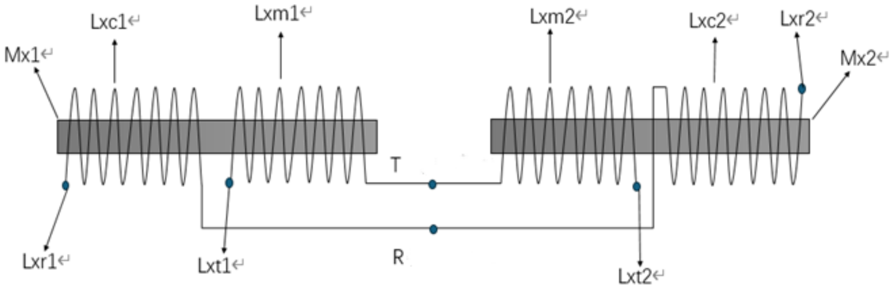

Fig 6. Schematic diagram of the X-axis coil framework

4. Simulation Analysis and Feasibility Testing

To verify the feasibility of the design during the design phase, this paper uses finite element simulation software to create a three-dimensional finite element model of the sensor for electromagnetic simulation.

4.1. Simulation Modeling

To balance computational accuracy and efficiency, two optimizations were applied to the simulation model. First, the actual densely wound coil was approximated as a uniform coil region; this model accurately calculates the macro-scale electromagnetic effects of the coil while avoiding the extremely high computational cost associated with the physical helical structure. Second, given that the relative permeability of the PEEK frame material is close to 1 and its electrical conductivity is extremely low—making its electromagnetic properties highly similar to those of air—its geometric structure was omitted. These two simplifications significantly reduced model complexity while ensuring the accuracy of the magnetic circuit and spatial gradient field analysis, thereby improving mesh quality and solution stability. Key simulation parameters are shown in Table 2:

Table 2. Key simulation parameters

Parameters	Conductivity(S/m)	Relative magnetic permeability	Number of turns (turns)
Magnetic core	10e6	10000	\
Excitation coil	5.998e7	1	200
Receiving coil	5.998e7	1	300

4.2. Static Performance Validation

The simulations in this phase are designed to abstract away the sensor's complex circuitry and operating mechanisms, focusing instead on verifying the inherent characteristics of its mechanical structure and differential configuration. All simulations are conducted under "steady-state" conditions, with the excitation coil current set to zero to simulate the sensor's passive detection state.

To evaluate the sensor's ability to suppress a uniform ambient magnetic field, a global uniform background magnetic flux density field of 50 μT in the Z-axis direction was applied in the "Magnetic Field" interface to simulate a typical geomagnetic field environment. The simulation results are shown in Figure 7. The normal components of the magnetic flux density at two symmetric points on the two symmetric cores (Mx1, Mx2) along the sensor's X-axis were extracted. The calculation results show:

$$|B_{X+} - B_{X-}| \le 0.1\mathrm{n}T \qquad (6)$$

This value approaches zero, which directly confirms, from the perspective of fundamental electromagnetic principles, that the centrally symmetric differential structure proposed in this paper can achieve first-order physical suppression of a uniform background magnetic field, thereby laying a solid hardware foundation for the sensor's high resistance to interference.

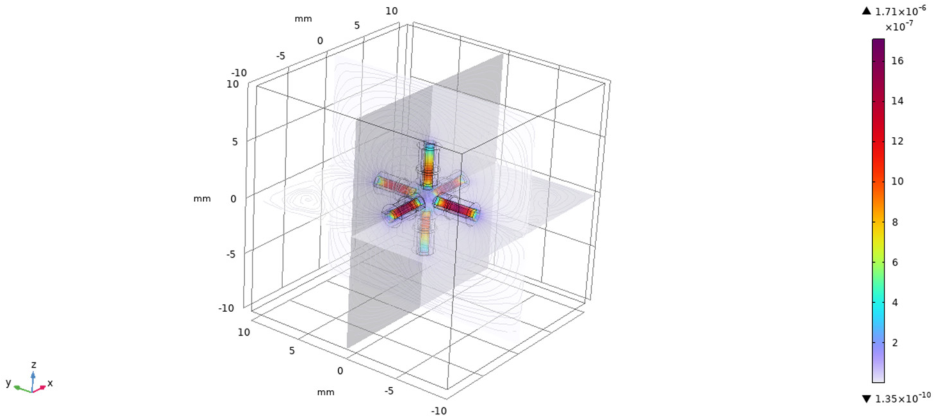

Fig 7. Uniform field simulation results

radius of 1 mm was introduced 10 mm from the sensor along the X-axis as a magnetic target. By assigning the sphere the properties of a uniformly magnetized material with a magnetic moment (M_z) along the Z-axis, it can be treated as a magnetic dipole, thereby generating a controllable, non-uniform gradient magnetic field in space. To comprehensively evaluate the response characteristics, a parametric scan was performed with M_z = [1e5, 5e5, 1e6, 2e6, 5e6] A/m to systematically vary the gradient field strength. The simulation results are shown in Figure 8.

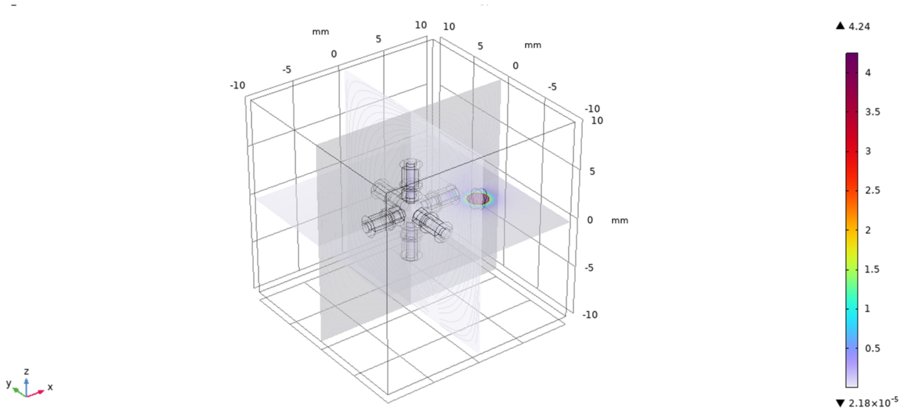

Fig 8. Gradient response simulation results

For each scanning step, the sensor output data is calculated, and the difference in the normal component (Bz) between the two magnetic cores along the X-axis is extracted; this difference represents the simulated sensor output. At the sensor's center point O, the true theoretical magnetic field gradient is calculated using the finite difference method. All obtained data points are plotted as a scatter plot and linearly fitted, as shown in Figure 8.

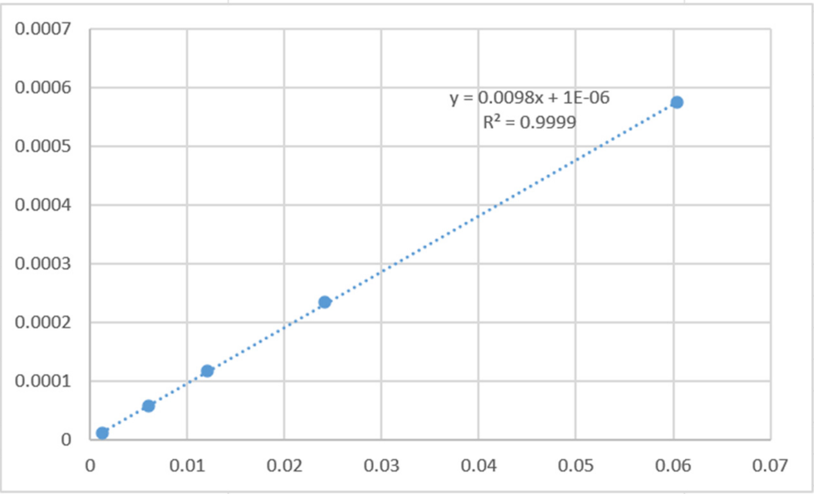

Fig 9. Gradient data scatter plot

The fitting results show that the data points align closely with the fitted line, with a linear correlation coefficient of $R^2>0.999$, indicating excellent linearity of the sensor within the test range. The slope of the fitted line represents the sensor's gradient sensitivity. Theoretically, for an ideal differential sensor with a baseline length of 10 mm, its sensitivity should equal the baseline length. The sensitivity measured in this simulation is 9.8 mm, with a relative error of less than 2% compared to the theoretical value. This result not only verifies the sensor's effective response to gradient fields but also precisely calibrates its sensitivity, demonstrating a high degree of consistency between the electromagnetic and structural designs.

4.3. Analysis of Frequency-Domain Operating Conditions

The simulation in this phase is designed to replicate the sensor's actual operating conditions after power-up. A "frequency-domain" analysis is employed, with the frequency set to 10 kHz, and a corresponding sinusoidal AC current applied to the excitation coil.

To evaluate the level of electromagnetic crosstalk between the sensor's three axes, a separate simulation was conducted with the aforementioned AC excitation applied only to the X-axis excitation coil; the simulation results are shown in Figure 10.

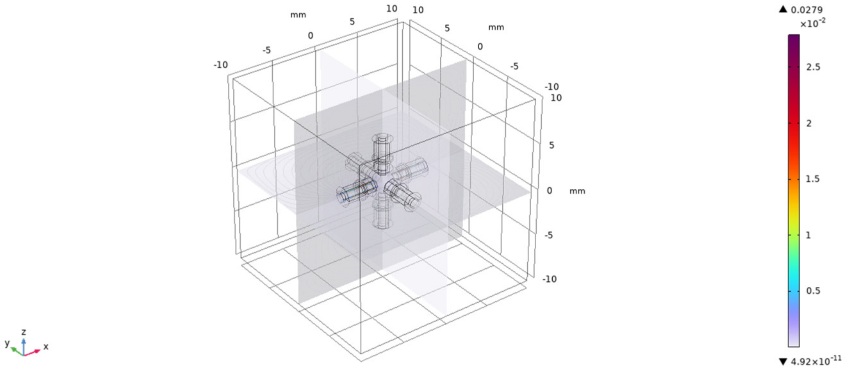

Fig 10. Simulation diagram of triaxial electromagnetic crosstalk

Simulation results indicate that when only the X-axis is excited, the induced magnetic field strengths along the Y and Z axes are four orders of magnitude lower than the main magnetic field along the X-axis. This result demonstrates that magnetic coupling between the three axes is extremely weak, and crosstalk is effectively suppressed, thereby ensuring the independence of each measurement channel and laying the foundation for high-precision decoupled measurement of three-dimensional vectors.

To simulate the sensor's performance under real-world operating conditions, a comprehensive scenario simulation was conducted. The excitation coils for the X, Y, and Z axes were activated simultaneously, and a ferromagnetic target was placed at the spatial coordinates (5, -5, 0) mm to the side of the sensor. The simulation results are shown in Figure 11:

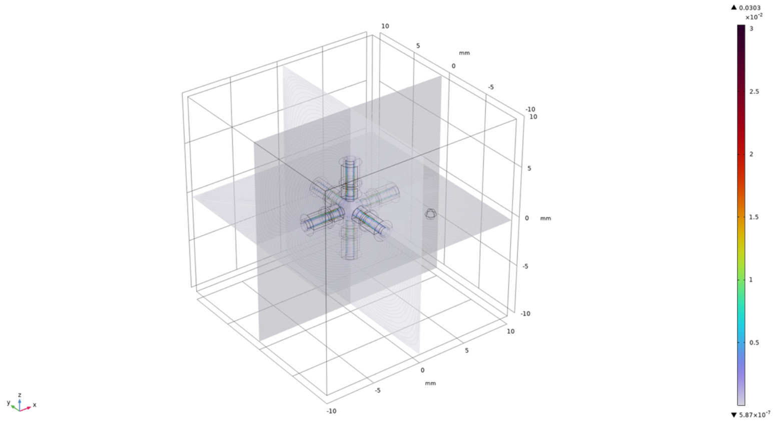

Fig 11. Simulation of a triaxial orthogonal sensor

Simulation results show that by combining the fundamental wave amplitudes of the extracted three-axis magnetic fields and calculating the resulting differential signals, data analysis indicates that when a target is present, all three sensor axes output significant and distinct differential signals. This result is qualitatively consistent with the static principle that "a target generates a spatial gradient field." This demonstrates that when the sensors operate in multi-axis synchronized mode, they can effectively detect gradient fields, thereby preliminarily validating their functional effectiveness in simulated real-world detection scenarios.

5. Summary

This paper presents a detailed design of an innovative three-dimensional orthogonal magnetic gradient sensor. Through an integrated mechanical structure and differential mechanism, it addresses several issues inherent in traditional discrete gradient sensors at the physical level. Both theoretical analysis and finite element simulation results indicate that this design can effectively suppress common-mode interference in principle and ensures high consistency across the three-axis measurement units, demonstrating the potential for high-precision and high-stability measurements. This design offers a novel hardware implementation approach for magnetic gradient measurement. Future work will focus on the precision machining and assembly of sensor prototypes, as well as the establishment of a standard testing platform. Comprehensive experimental calibration of key performance metrics—including sensitivity, background noise, linearity, and temperature stability—will be conducted to ultimately quantify the performance advantages of the sensor and facilitate its practical application.

References

[1] Wang Yanzhang, Ji Cheng, Li Jisheng, et al. Design of a Homodyne Even-Order Harmonic Fluxgate Magnetic Gradiometer[J]. Journal of Instrumentation, 2019, 40(01):85-91.

[2] Yang Zhicheng, Yan Shenggang, Li Bin. Research on the Calibration Algorithm of Three-Component Fluxgate Gradiometer[J]. Journal of Instrumentation, 2017, 38(08):2055-2061. 2017.08.026.

[3] Gao Xiang, Yan Shenggang, Li Bin. Method for Correcting Magnetic Flux Gate Gradiometer Heading Difference Based on Least Squares[J]. Journal of Northwestern Polytechnical University, 2016, 34 (05): 837-842.

[4] China Aerodynamics Research and Development Center, Institute of Hypersonic Aerodynamics. Cross-shaped variable-baseline fluxgate array and method for measuring the third-order magnetic gradient tensor: 202511072114.1[P].2025-10-17.

[5] Chengdu University of Technology. Flux Gate Gradient Measurement Probe: 201810363930.1[P]. 14 July 2020.

[6] Nanjing Maikoni Sensor Technology Co., Ltd., Changzhou Micromagnetic Amorphous Wire Sensor Co., Ltd. A high-resolution orthogonal fluxgate omnidirectional magnetic field gradient sensor based on an orthogonal array of amorphous wires: 201810280585.5[P]. 31 August 2018.

[7] Zhi Menghui. Research on High-Precision Digital Fluxgate Sensors [D]. Soochow University, 2017.

[8] Li Chao. Design and Implementation of High-Precision Single-Axis Fluxgate Sensor[D]. Harbin Engineering University, 2011.

[9] Yang Shanglin, Liu Shibin, Guo Bo, et al. Analysis of the Influence of Core Parameters on the Input and Output Characteristics of Fluxgate[J]. Journal of Sensing Technology, 2014, 27(01):40-47.

[10] Tu Chuanbin. Research on Weak Magnetic Field Detection Technology Based on Fluxgate Sensors [D]. Shenyang University of Technology, 2013.

[11] Jiao Xiongfeng. Research on Triaxial Fluxgate Sensors and Their Application in Attitude Measurement [D]. North China Institute of Technology, 2001.

[12] Gao Zili, Wang Yu. Design of Signal Sources Based on DDS Technology[C]//Tianjin Electronics Industry Association. Proceedings of the 2020 Annual Conference of Tianjin Electronics Industry Association. Zhonghuan Leading Semiconductor Materials Co., Ltd.; 2020:40-43.

[13] Yang Yuxiang, Wang Jue, Niu Feilong, et al. Design of a sinusoidal frequency-sweeping constant current source [J]. Journal of Instruments, 2006,(S1):162-164. 2006.